Title

Prediction of vortex shedding suppression from circular cylinders at high Reynolds number using base splitter plates

Permalink

https://escholarship.org/uc/item/9w9473m0

Authors

Dai, Shaoshi
Younis, Bassam A
Zhang, Hongyang
et al.

Publication Date

DOI

Prediction of vortex shedding suppression from circular cylinders at high Reynolds number using base splitter plates

Shaoshi Dai [a,*], Bassam A. Younis [b], Hongyang Zhang [a], Chunyu Guo [a]

[a] *Deep Water Engineering Research Center, Harbin Engineering University, 150001, China*
[b] *Department of Civil & Environmental Engineering, University of California, Davis, CA, 95616, USA*

A B S T R A C T

Computations were performed to determine the optimal conditions for the suppression of vortex shedding from circular cylinders at high Reynolds number by means of splitter plates. Previous studies of this mechanism for vortex-shedding control have largely been confined to two-dimensional flows at low Reynolds number, and to a single ratio of splitter plate width to cylinder diameter. In this study, we consider fully-turbulent, three-dimensional flows at high Reynolds number, and investigate the dependence of vortex-shedding suppression on two geometric parameters; namely the ratio of splitter-plate width and height to cylinder diameter and length. The computations were performed with the OpenFOAM software using a well-validated turbulence closure that considers the effects of the organized mean-flow unsteadiness on the random turbulent fluctuations. Comparisons were made with experimental data, and the validated method is used to perform a systematic study to determine the effectiveness of vortex suppression. To aid in the analysis, two-point correlations of forces along span of cylinder were obtained to determine uncoupling conditions of sectional oscillations. The results obtained indicate that splitter plates provide a practical method for vortex suppression at high Reynolds number, and the degree of suppression can be maximized by optimal geometric configuration.

1. Introduction

The ever-growing interest in sustainable energy generation from wind turbines places greater demands on our ability to accurately predict and control the unsteady aerodynamics and hydrodynamic forces associated with vortex shedding from circular cylinders at high Reynolds numbers. The particular application that motivated the present study relates to the rapid increase in the installation of wind turbines on fixed and floating offshore platforms (EWEA, 2017; Tran and Kim, 2015; Feyzollahzadeh et al., 2016). In these applications, the main supporting structure for the wind turbine is in the form of a circular tower which, in shallow waters, is installed on a fixed support such as a monopile foundation and, in deeper waters, on a floating semi-submersible platform. In either case, the tower and its support are vulnerable to fatigue damage due to the occurrence of vortex shedding by wind and current. Choi et al. (2008) present a comprehensive review of methods for the control of vortex shedding by passive and active means. Active-control methods include base-flow suction (Chen, 2013), base-flow blowing (Schumm, 1994), moving surface boundary-layer control (Korkischko and Meneghini, 2012), electrical heating of cylinder surface (Lecordier, 1991), rotary oscillating

control (Tokumaru, 1991) and optimal control (Homescu, 2002). While the effectiveness of these methods has been amply demonstrated in small-scale laboratory experiments at low Reynolds number, none have found use in practice due to their complexity, lack of resilience, and excessive energy demands. This last constraint is entirely absent from passive-control methods as these achieve the intended results entirely via suitable modification of the cylinder geometry (Zdravkovich, 1981). Several alternative methods have been reported in the literature. These include the use of ribbons (Kwon, 2002), helical strakes (Bearman and Branković, 2004; Trim, 2005), fins (Yeung, 2002), and base splitter plates (Apelt et al., 1973; Unal and Rockwell, 1988). Of these, the most-widely used method in offshore engineering has been the helical strakes. These, however, while being robust and effective in a wide range of conditions, are known to increase the overall drag (Blevins, 1990). Thus the search for an alternative, passive method for vortex shedding control continues, increasingly centered on the use of computer simulations to explore the effectiveness of such a method at the high Reynolds numbers typically obtained in practice. Our interest in base splitter plates is motivated by a number of considerations that include the relative ease of their deployment on existing large-scale offshore wind-energy installations, their

---

resilience to self-induced fatigue, and to the cost effectiveness of their manufacture and installation compared to helical strakes. The fact that splitter plates are mainly effective in flows that are directed at zero incidence to their axis is of no concern for offshore wind turbines where the direction of the prevailing wind, being virtually always onshore, is known *a priori*. In environments where the angle of incidence can vary over a considerable range, the splitter plate may be mounted, in the manner of a "wind vane", on a rotating sleeve so as to restore alignment (Gu et al., 2012). The principal aim of this study was to quantify, by means of systematic computations, the optimal geometric parameters that maximize the effectiveness of base splitter plates in fully-turbulent flows at high Reynolds number. The ultimate goal is to provide guidance regarding the implementation of these devices in practice. In what follows, we outline the computational methodology focusing on the representation of the effects on turbulence due to the presence of vortex shedding. This is followed in Section 3 by the presentation and discussion of the results including assessment of their numerical accuracy, and their implications regarding the optimal configuration of the splitter plate with respect to the cylinder dimensions. Conclusions arising from this study are presented in Section 4.

2. Computational details

In deciding on the methodology for the prediction of three-dimensional unsteady turbulent flows of engineering interest, the choice to be made is between using Large-Eddy Simulations (LES), and what is commonly referred to as Unsteady Reynolds-Averaged Navier-Stokes (URANS). The computational demands of LES are quite severe: the numerical grid is required to be sufficiently fine for the resulting control volumes to be small enough to capture most of the energy-bearing eddy motions. When this requirement is coupled with the Courant condition for the stability of explicit differencing schemes, the result is a time-step size that is very small compared to the time scale of the vortex shedding process. In contrast, in the URANS approach, the size of both the time step and the control volumes is determined by the requirement that the solutions obtained are sensibly free of dependence on grid/time-step sizes. In this study, and bearing in mind that the focus is mainly on global parameters such as the lift and drag coefficients rather than on detailed examination of the physical processes involved, the choice was made to use the URANS approach to solving the equations that govern the conservation of mass and momentum in turbulent flow conditions. In this approach, the instantaneous equations are averaged over a time interval equivalent to the computational time step (Δt). The resulting equations can be written, using conventional Cartesian tensor notation, as:

$$\frac{\partial U_i}{\partial x_i} = 0 \tag{1}$$

$$\frac{\partial U_i}{\partial t} + U_j \frac{\partial U_i}{\partial x_j} = \frac{\partial}{\partial x_j}\left(\nu \frac{\partial U_i}{\partial x_j} - \overline{u_i u_j} \right) - \frac{1}{\rho}\frac{\partial p}{\partial x_i} \tag{2}$$

Where U_i is the mean-velocity vector, u_i is the fluctuating velocity, p is the mean pressure, ν and ρ are, respectively, the kinematic viscosity and density.

The unknown turbulence correlations C_d that appear in Eq. (2) are obtained from Boussinesq's linear stress-strain relationship:

$$-\overline{u_i u_j} = \nu_t \left(\frac{\partial U_i}{\partial x_j} + \frac{\partial U_j}{\partial x_i} \right) - \frac{2}{3}\delta_{ij} k \tag{3}$$

where k is the turbulence kinetic energy and ν_t is the eddy viscosity which is obtained from:

$$\nu_t = C_\mu \frac{k^2}{\varepsilon} \tag{4}$$

The quantities k and ε (the viscous dissipation rate) are obtained from the solution of their own transport equations:

$$\frac{\partial k}{\partial t} + U_j \frac{\partial k}{\partial x_j} = \frac{\partial}{\partial x_j}\left(\left(\nu + \frac{\nu_t}{\sigma_k} \right) \frac{\partial k}{\partial x_j} \right) + P_k - \varepsilon \tag{5}$$

$$\frac{\partial \varepsilon}{\partial t} + U_j \frac{\partial \varepsilon}{\partial x_j} = \frac{\partial}{\partial x_j}\left(\left(\nu + \frac{\nu_t}{\sigma_\varepsilon} \right) \frac{\partial \varepsilon}{\partial x_j} \right) + C_{\varepsilon 1}\frac{\varepsilon}{k}P_k - C_{\varepsilon 2}\frac{\varepsilon^2}{k} \tag{6}$$

where $C_{\varepsilon 1}$, $C_{\varepsilon 2}$, σ_k, σ_ε and C_μ are model constants assigned here their standard values (viz. 1.45, 1.90, 1.0, 1.3, 0.09) and P_k is the rate of production of turbulence kinetic energy:

$$P_k = -\overline{u_i u_j}\frac{\partial U_i}{\partial x_j} \tag{7}$$

It has been demonstrated in numerous previous studies that the standard $k-\varepsilon$ model as presented above fails to capture the occurrence and strength of vortex shedding from cylinders (Murakami, 1993; Tsuchiya et al., 1997). The reasons for this are not entirely clear and have variously been attributed to such factors as the use of the standard logarithmic law of the wall to provide the boundary conditions around the cylinder (Franke and Rodi, 1993), and to the inability of Boussinesq's relation to properly account for the effects of normal strains on the rate of production of turbulence kinetic energy (Kato and Launder, 1993). In experiments on turbulent vortex shedding from cylinders where the turbulence energy spectrum was reported, a discrete peak in the spectrum in the inertial sub-range is clearly observed, occurring at a frequency that exactly matches the shedding (Strouhal) frequency (Durao et al., 1988). The presence of this peak may be taken to suggest that the dissipation-rate equation, being formulated with the assumption of spectral equilibrium, does not properly account for the consequences of the interactions between the periodic mean-flow oscillations and the random turbulent motions. In effect, when vortex shedding is present, the turbulence kinetic energy is maintained by both a direct input of energy at the Strouhal frequency, as well as by the usual mechanism of the working of the turbulent shear stresses against the mean rates of strain (Eq. (7)). This mechanism was explored analytically by Younis and Zhou (2006) who postulated a form for the modified spectrum and proceeded to obtain an expression for its effect on the energy transfer process. The outcome was a recommendation for an extra term to be included in the dissipation rate equation to represent the effects of vortex shedding on the dissipation process. The proposed modification was subsequently tested in a wide range of flows that are strongly influenced by vortex shedding. These included the benchmark flow around isolated square and circular cylinders (Younis and Przulj, 2006), the flow around a full-scale Tension Leg Platform (Dai et al., 2015), and the flow around a square cylinder with rounded corners (Dai et al., 2017). In each case the results obtained with the modified model were distinctly better than those obtained with the standard formulation. This modification involves redefining the coefficient $C_{\varepsilon 1}$ in Eq. (6) thus:

$$C_{\varepsilon 1}^* = C_{\varepsilon 1}\left(1 + C_t \frac{k}{\varepsilon} \frac{1}{Q+k}\left| \frac{\partial(Q+k)}{\partial t} \right| \right) \tag{8}$$

where Q is the mean-flow kinetic energy per unit mass. The coefficient C_t is set equal to 0.38 as suggested in the original reference.

Equations (1)–(8) were solved by finite volume methodology incorporated in OpenFOAM. The convective fluxes were approximated using the Gauss van Leer V integral discrete lattice, while the Laplacian and pressure gradient terms were discretized using the Gauss linear corrected scheme. The temporal terms were discretized by using the implicit second-order accurate backward lattice scheme. A multi-block solution methodology was adopted wherein the computational domain was subdivided into a number of blocks with each block meshed separately. This was done to obtain computational efficiency on multi-core processors, to better define the surface geometry and to concentrate the

mesh in the flow regions where the variations are rapid. The solution procedure was iterative and the convergence criterion for the iterative process at each time step was set to be when absolute sum of all residuals fell to a value below 10^{-6}.

3. Results and discussion

We first assess the modified turbulence model by comparisons with data for the flow around a circular cylinder with no splitter plates. This is a standard benchmark test case for flows with vortex shedding (e. g. Murakami, 1993). The computational grid and the solution domain are shown in Fig. 1.

In the two-dimensional simulations, a single cell was used in the spanwise direction. A structured hexahedral mesh was generated using the ICEM-CFD software which is interfaced with OpenFOAM. In constructing the grid, care was taken to ensure that the near-wall region was adequately resolved. To this end, the number and distribution of the grid nodes was adjusted so that the normal distance from the center of all cells in contact with the cylinder surface to the cylinder surface itself was 1.38×10^{-3}. In wall coordinates, this amounted to ensuring that y^+ was constrained to remain at a value below 30. The location of the cylinder with respect to the boundaries, and the resulting blockage ratio of less than 10%, were found not to influence the predicted forces on the cylinder (Younis and Przulj, 2006). The boundary conditions were as follows: at inlet, a uniform velocity was prescribed consistent with the required Reynolds number ($Re = 1.8 \times 10^5$ for this case). The turbulent kinetic energy was specified based on an assumed value of the relative turbulence intensity at inlet of 0.5%. This value is representative of those found at inlet to the test section of a water flume or a wind tunnel, and is necessary to maintain a finite level of turbulence kinetic energy in the region of the flow upstream of the cylinder where the mean velocity would still be uniform and hence the rate of production of k would be effectively zero (Eq. (7)). Batham (1973) reported on the effects of free-stream turbulence on the mean and fluctuating pressure on the surface of long circular cylinders having smooth and rough surfaces, at Reynolds numbers of 1.1×10^5 and 2.35×10^5 in both uniform and turbulent streams. For the case of a smooth surface, these were found to suppress vortex shedding from the cylinder. An important consequence of elevated levels of free-stream turbulence is the triggering of laminar-turbulent transition in the boundary layer. Such effects are not reproducible by the high Reynolds-number turbulence closure employed in this study wherein the flow is assumed to be turbulent throughout the computational domain. Hence the prescription of a level of turbulence intensity at inlet to the computational domain that is higher than that obtained in experiments will thus remain a source of uncertainty in the computations. The dissipation rate was obtained from Eq. (4) by setting the ratio of eddy to molecular viscosity to 100. This is done also in order

to keep the dissipation rate finite upstream of the cylinder due to the absence of mean shear there. At the exit, fully-developed flow conditions were assumed so that the streamwise gradients of all dependent variables were set to zero. The cylinder walls were taken to be smooth, and in specifying the boundary conditions around the cylinder, it was assumed that the velocity component parallel to the wall and at the nodes closest to it followed the universal logarithmic law of the wall:

$$\frac{U}{u_\tau} = \frac{1}{\kappa} \ln \left(E \frac{u_\tau \Delta y}{\nu} \right) \tag{9}$$

where u_τ is the friction velocity and Δy is the normal distance from wall to the grid nodes in contact with it. This allowed the 'wall function' approach to be adopted wherein the momentum flux at the wall was deduced from Eq. (9), while the values of the turbulence kinetic energy and its rate of dissipation were fixed based on the assumption of local equilibrium. The constants E and κ (the von Karman constant) were assigned their usual values of 9.8 and 0.41, respectively.

To check for dependence of the computed results on the numerical grid, computations were performed on three different grids in order to obtain an estimate of the discretization errors using the Grid Convergence Index (GCI) method (Celik et al., 2008). The outcome of these computations is presented in Table 1. The three grids, which were refined approximately in the ratio 1.1, consisted of 110087, 131946 and 156565 active cells in which the number of cells that were in direct contact with the cylinder surface was 100, 160 and 240, respectively. The solutions obtained were then used to calculate the apparent order of accuracy of the method, and the extrapolated values (φ_{ext}^{21}) which together yielded the value of the fine-grid convergence index (GCI_{fine}^{21}). It can be seen from Table 1 that the numerical uncertainty in the fine-grid results for the three variables examined (namely the mean and fluctuating force

Table 1
The GCI method estimates of discretization errors.

Variables/Coefficients	$\varphi_1 = C_d$	$\varphi_2 = C'_d$	$\varphi_3 = C'_l$	$\varphi_4 = St$
N_1, N_2, N_3	156565 (240) , 131946 (160) , 110087 (100)			
γ_{21}	1.089			
γ_{32}	1.095			
φ_1	0.969	0.147	0.737	0.208
φ_2	0.988	0.146	0.730	0.210
φ_3	1.028	0.149	0.742	0.185
p	7.838	14.22	6.258	33.182
φ_{ext}^{21}	0.949	0.147	0.746	0.184
e_a^{21}	0.020	0.005	0.009	0.134
e_{ext}^{21}	0.021	0.002	0.013	0.008
GCI_{fine}^{21}	0.026	0.003	0.016	0.010

Note: Numbers in brackets represent the number of mesh points in direct contact with the cylinder.
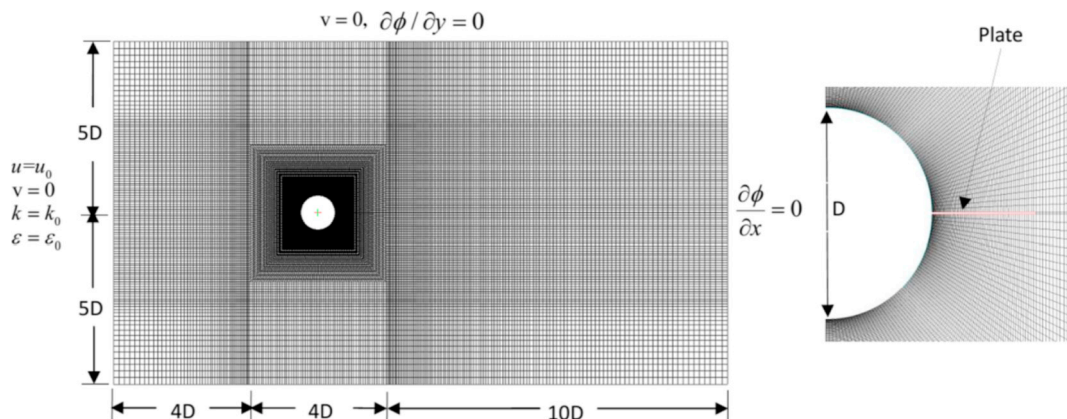

Fig. 1. Grid, boundary conditions and solution domain.

coefficients and the Strouhal number) amounts to under 3% of the asymptotic values. Hence the mesh consisting of 156,565 active cells was adopted for all subsequent calculations.

Fig. 2 presents a comparison of the predicted and measured mean and fluctuating wall static pressure distribution around the cylinder. It can be seen that overall, with the modified model, the predicted distribution of *Cp* is in better agreement with the measurements of Qiu et al. (2014) and Cantwell and Coles (1983), especially downstream of the separation point. This is also the case for the predicted fluctuating pressure coefficients shown in Fig. 2 where it is evident that the standard model seriously underestimates this parameter. It should be noted that both the numerical and experimental results are at Reynolds numbers close to the critical regime and this will have contributed to the observed discrepancies and scatter.

Attention is turned next to the computation of the two-dimensional flow around a circular cylinder with a splitter plate attached to its base. It is to be expected that the ratio of the splitter plate width (*w*) to the cylinder diameter (*D*) would be a critical parameter in determining the effectiveness of this approach in suppressing the vortex shedding and hence the resulting unsteady forces on the cylinder. The extent to which the overall flow field is modified by the presence of the splitter plate can be seen in Fig. 3 which shows the predicted contours of vorticity obtained for the case without a plate, and for the case where $w/D = 1.0$. These results were obtained with the modified turbulence model. For the case of $w/D = 0$, a classic wake structure with periodically alternating vortices is observed wherein the shear layers that form on either side of the cylinder begin to interact close to the surface resulting in strong alteration of the pressure field around the cylinder and hence large fluctuations in the lift and drag forces. For the case where $w/D = 1.0$, the vortices appear to roll on to the surface of the plate before being connected downstream. Also apparent is the presence of regions where vorticity of opposite sign coexist side by side on either side of the splitter plate. The coupling between the ones shed from above or below the plate is much weakened and with it, as will be seen later, the oscillations in the pressure field.

Comparisons are made with the limited experimental data that are available for this purpose (West and Apelt, 1993; Anderson and Szewczyk, 1997). These are for two values of *Re*, namely 2.0×10^4 and 4.6×10^4, and for a splitter width to diameter ratio c of 0.25 and 0.21, respectively. The predicted variation of mean wall static pressure with angle is presented in Fig. 4 where the results are compared with the data of West and Apelt (1993) and Anderson and Szewczyk (1997). It can be seen there that the predicted circumferential distribution of *Cp* is generally in reasonable accord with the experimental results from West and Apelt (1993) considering the extent of scatter observed in the latter. Regarding the distribution of the fluctuating wall static pressure on the cylinder with a splitter plate, very little has been published in the open literature. Gu et al. (2012) studied the influence of rotatable splitter

plates on loading on a circular cylinder and reported on some measurements of the circumferential distribution fluctuating pressure coefficients with different plate lengths. Comparisons with their measurements are presented in Fig. 4. The correspondence between predictions and measurements is generally quite satisfactory although the peak value of this parameter appears to be somewhat over predicted.

It is instructive to examine the dependence of wall static pressure distribution on w/D even though experimental data are not available for comparisons. The mean and r.m.s. values of the pressure coefficient are obtained by time averaging their instantaneous $\left(C_p(t) = \frac{p-p_\infty}{0.5\rho u_0^2} \right)$ and fluctuating values $C_p'(t) = \left(\frac{p-\bar{p}}{0.5\rho u_0^2} \right)$. Fig. 5 shows the variation of C_p with w/D as obtained with the modified turbulence model. For the case of $w/D = 0$, the base pressure coefficient (i.e. at $\theta = 180°$) is at its lowest value of around -1.12. The addition of splitter plates appears to initially monotonically increase this value but a plateau is reached for values of w/D greater than about 0.75 beyond which C_p appears to decrease with further increase in plate width. A similar behavior is observed for the fluctuating surface pressure distribution which is also shown in Fig. 5. For $w/D = 0$, the fluctuating pressure coefficient C_p' reaches a maximum of about 0.55 at a turning angle (θ) of about 90°. With the splitter plates attached, C_p' seems to again initially reduce to reach a plateau only to increase again for values of $w/D > 0.5$.

From an engineering standpoint, the main interest is in the consequences of adding splitter plates on the time-averaged mean drag, and on the root mean square values of lift and drag. These quantities are evaluated by time averaging their instantaneous values which, in turn, are obtained as follows:

$$C_d(t) = \frac{1}{2}\int_0^{2\pi} C_p(t)\cos\theta d\theta, \; C_d'(t) = \frac{1}{2}\int_0^{2\pi} C_p'(t)\cos\theta d\theta, \; C_l'(t)$$

$$= \frac{1}{2}\int_0^{2\pi} C_p'(t)\sin\theta d\theta$$

Fig. 6 displays the variation of mean and fluctuating drag coefficient with w/D. Note that these coefficients relate solely to the contributions due to pressure, the viscous component being relatively small and not typically reported in experimental studies. Two observations are immediately apparent. First, the presence of splitter plate causes both quantities to drop quite considerably (by as much as 35% for the case of C_d) relative to their original values. The drop in C_d', the fluctuating drag coefficient, is even more pronounced but this parameter is of relatively minor importance in engineering design. Second, the variation in C_d is far from being monotonic: this parameter drops to its lowest value in the range $0.5 < w/D < 0.75$ before rising again. In contrast, the C_d' value appears to reach a plateau before decreasing sharply for values of w/D greater than 1.0 $w/D = 1.25$.
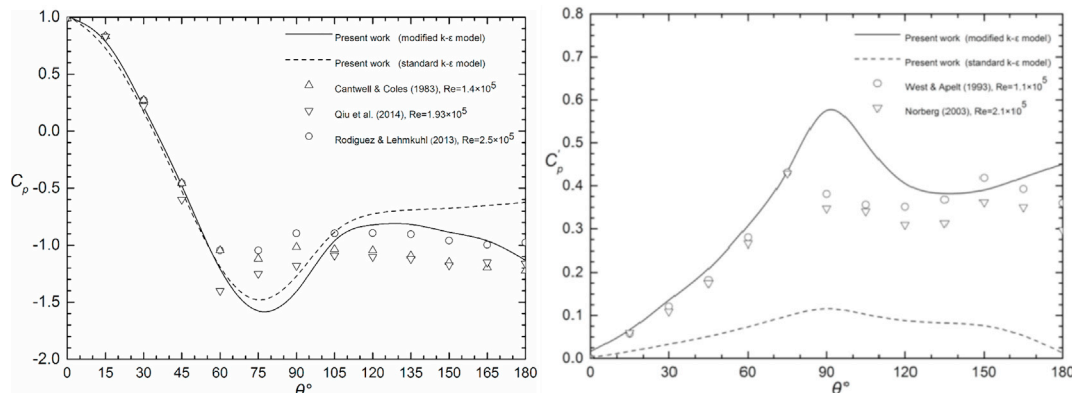

Fig. 2. Predicted and measured mean (left) and fluctuating (right) surface pressure distribution (Norberg, 2003; Rodríguez and Lehmkuhl, 2013).
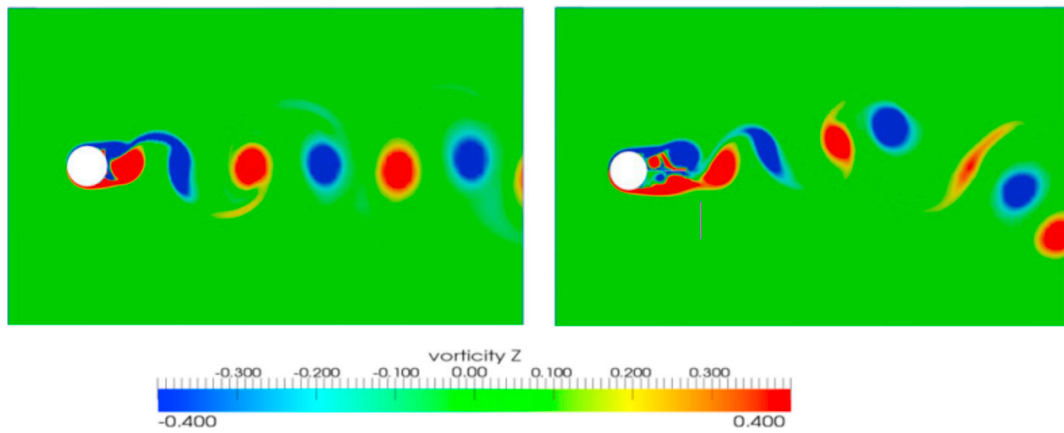
Fig. 3. Computed instantaneous vorticity contours for bare cylinder (left), and cylinder with splitter plate ($w/D = 1$) (right).
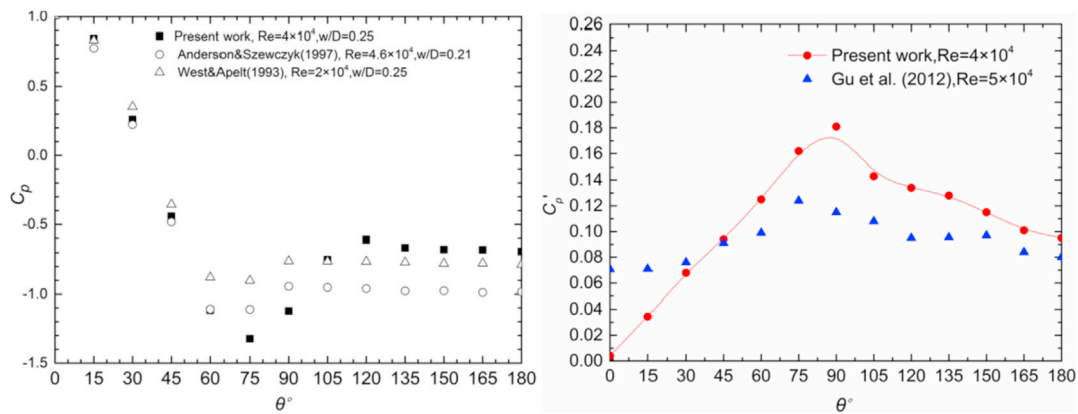

Fig. 4. Predicted and measured mean (left) and fluctuating (right) wall static pressure coefficients.
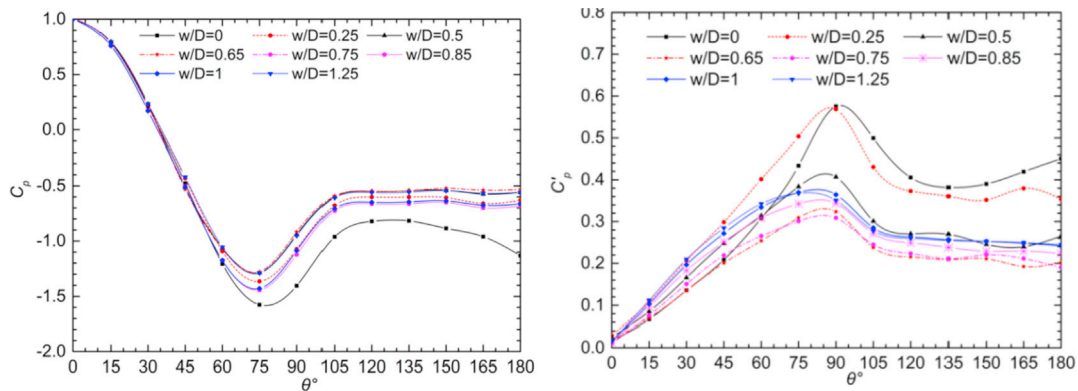

Fig. 5. Variation of mean (left) and fluctuating (right) wall static pressure coefficients with w/D.

The variation of the fluctuating lift coefficient with w/D is shown in Fig. 7. A similar behavior is observed: an initially steep drop followed by a plateau with the minimum value again occurring in the w/D range of 0.5–0.75. Taken together, the results suggest that the optimal value for w/D for maximum reduction in vortex shedding strength lies in this range. Within the studied range of $0 \leq w/D \leq 1.25$, the average percentage reduction of mean drag coefficient, fluctuating drag and lift coefficients is up to 30%, 80% and 20%, respectively (see Table 2).

Attention is turned now to consideration of the effects of a splitter plate on the forces that arise in a cylinder of small aspect ratio wherein the three-dimensional effects become important. Having determined from the results for the infinite aspect ratio case that the optimal ratio of

plate width to cylinder diameter is in the range $0.5 < w/D < 0.75$, we examine here the influence of plate height (H) to cylinder length (L) with the ratio varied in the range $0 < H/L < 1.0$ while w/D is held constant at 0.6. The cylinder aspect ratio (L/D) was fixed at 5.0. The geometry is shown in Fig. 8, and a representative grid in Fig. 9. For the fines mesh used, the total number of nodes in direct contact with the cylinder was 240 while the number of nodes in contact with the splitter plate was 96. In the horizontal planes, the grid is arranged in the same way as for infinite aspect ratio case while the vertical dimension that previously contained a single cell, is now resolved using 15 planes that yield a total of 815,260 active nodes. Comparative computations were performed with 26 cross-sectional planes. Some differences were observed in the
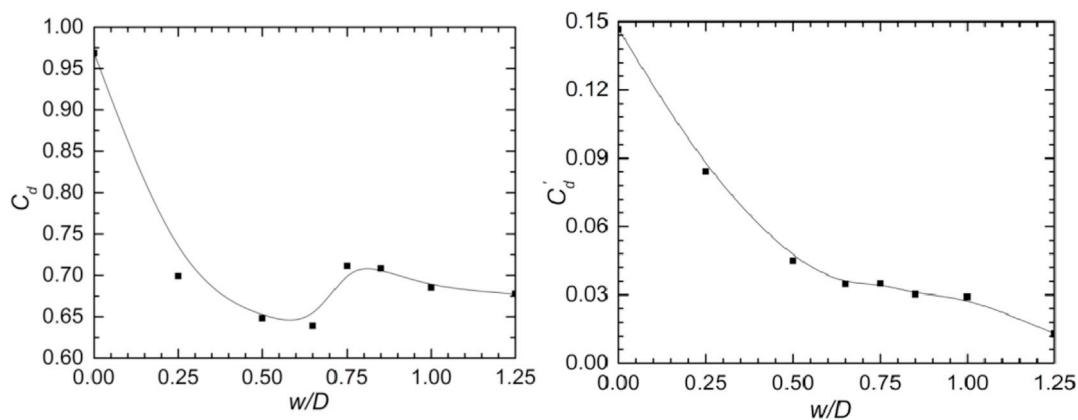
Fig. 6. Variation of mean (left) and fluctuating (right) drag coefficients with w/D.
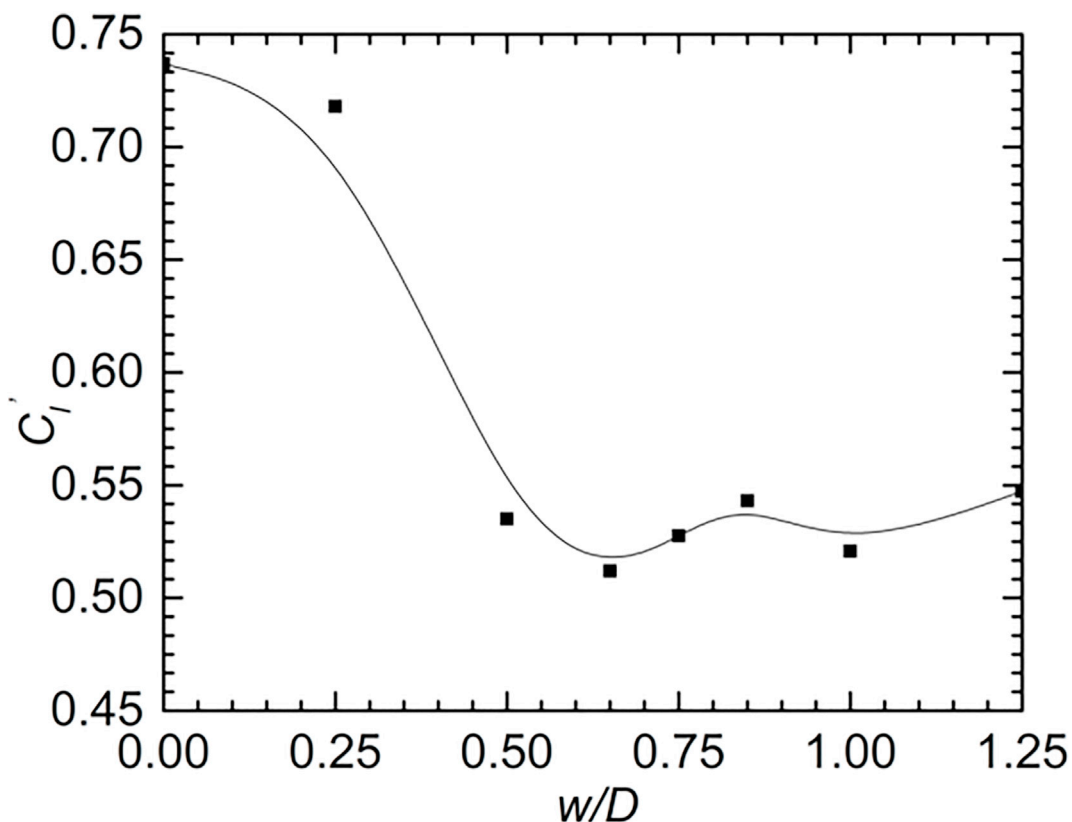

Fig. 7. Variation of the fluctuating lift coefficient with w/D.

contours of instantaneous vorticity in the neighborhood of the splitter plate/bare cylinder junctions but these differences were small and did not discernible differences in the long-time averaged wall static-pressure distributions, or in the bulk flow parameters C_l and C_d. The boundary conditions are as before with the side walls being treated as planes of symmetry. The non-dimensional computational time step Δt^* ($= \frac{U_0 \cdot \Delta t}{D}$) was set equal to 0.00261.

In the results that follow, the Reynolds number was set $Re = 1.8 \times 10^5$ and the splitter plate was located in the middle of the cylinder. In order to identify the effect of different H/L on sectional and integral force

Table 2
Force coefficients and their percentage reduction by splitter plate.

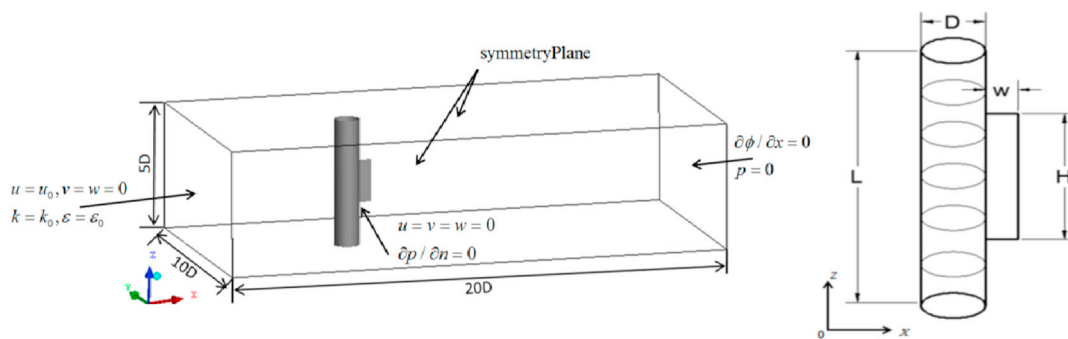| w/D	0	0.25	0.5	0.65	0.75	0.85	1.0	1.25
C_d	0.969	0.699	0.648	0.639	0.711	0.708	0.685	0.679
Reduction (%)	–	27.90	33.10	34.10	26.60	26.90	29.30	29.92
C_d'	0.147	0.084	0.045	0.035	0.035	0.030	0.029	0.013
Reduction (%)	–	42.86	69.39	76.19	76.19	79.59	80.27	91.16
C_l'	0.737	0.718	0.535	0.512	0.528	0.543	0.521	0.547
Reduction (%)	–	2.580	27.41	30.52	28.36	26.46	29.31	25.78

Fig. 8. Computational domain and boundary conditions for 3D simulations.
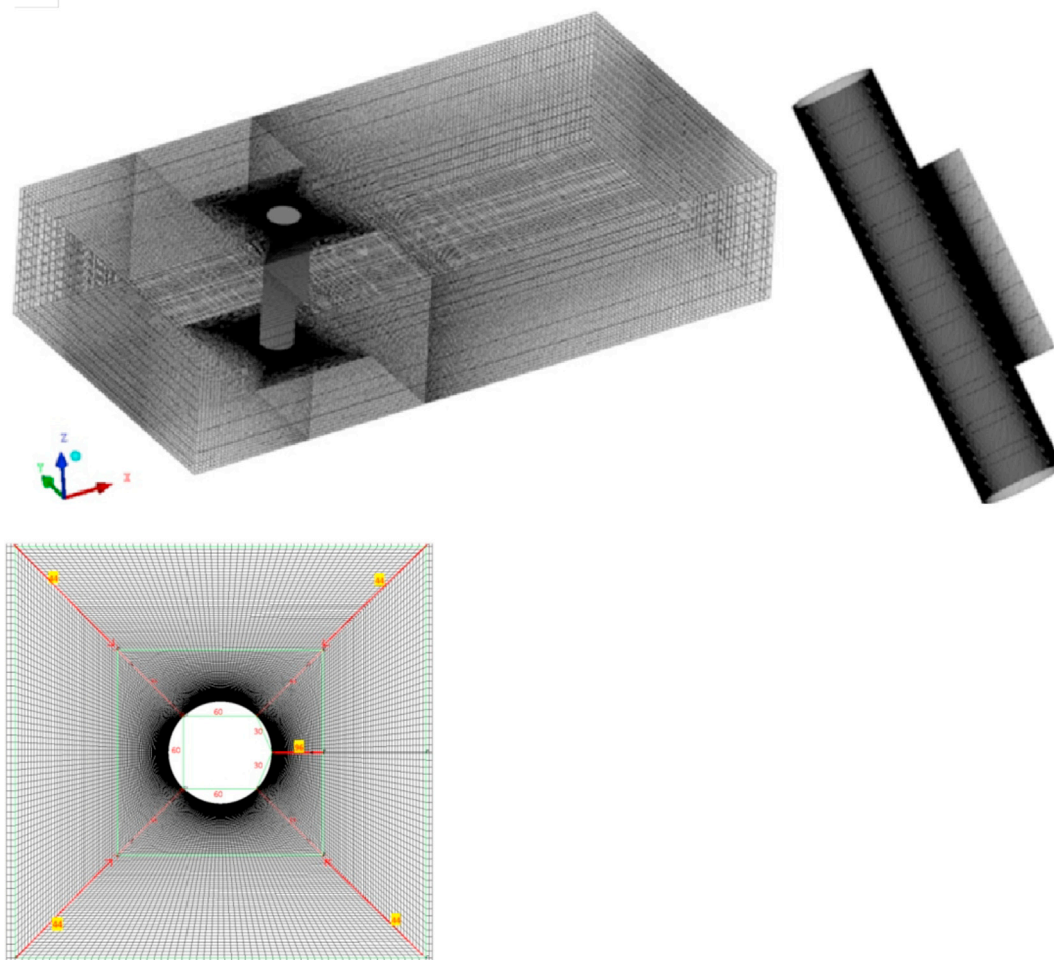

Fig. 9. Views of the 3D computational grid showing the number of cells employed around the cylinder and the splitter plate ($H/L = 0.5$).

coefficients and spanwise correlation, the cylinder was assembled from six monitoring segments and seven layers along the span of cylinder (Fig. 6). Along the circumference of cylinder, 24 monitoring points were set to obtain wall pressure.

In presenting the results for the lift and drag coefficients, the convention adopted here is to use lower case subscripts to denote sectionally-averaged quantities, and to use upper case subscripts to denote global values obtained by averaging the sectional values along the entire length of the cylinder. Fig. 10 shows the variation of C_d with distance along the length of the cylinder for several values of H/L. The strong dependence of the sectional drag on H/L is clearly evident, especially when contrasted with the values for the bare cylinder i.e. $H/$

$L = 0$. As expected, due to the three-dimensional nature of the flow over this small aspect ratio cylinder, the distribution along the cylinder length is both non-uniform and sensibly symmetric around the mid-section where the minimum values of sectional drag occurs for the cylinder with a splitter plate. For the bare cylinder, the sectional drag at the mid-plane is actually at a maximum which indicates that the addition of a splitter plate has induced large-scale alteration in the pressure field. This is clearly evident from Fig. 5 where the base pressure for the bare cylinder is much lower than that for any of the cases with a splitter plate indicating a greater net drag force and hence higher sectional drag coefficient.

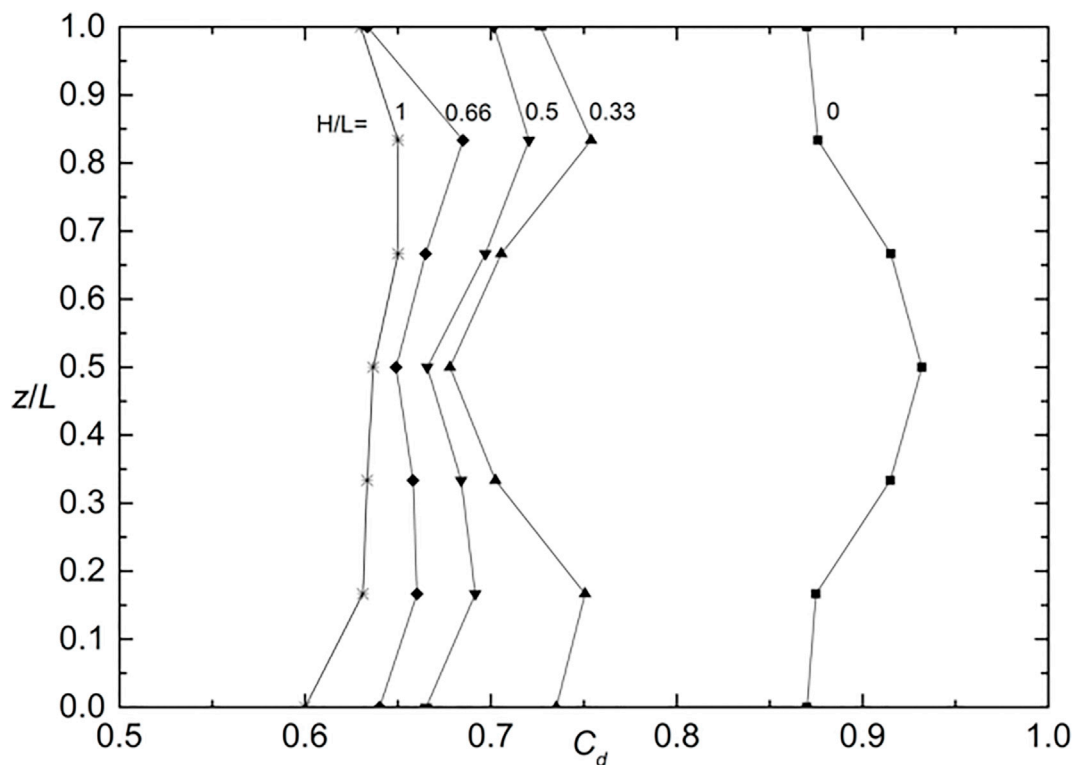The sectional values of the fluctuating drag and lift coefficients are

Fig. 10. Variation of sectional drag with splitter plate length.

presented in Fig. 11 where they are plotted against distance along the cylinder length with H/L as a parameter. For the case of $H/L = 0.66$, at the center plane of the cylinder, the fluctuating drag coefficient is reduced by a factor of 6, from 0.12 for the case with no splitter plate to 0.02. A notable feature of the change in the profile of C'_d with increasing H/L is the rounding off the discontinuity in slope that is evident in the $H/L = 0.33$ profile. This discontinuity arises from changes in the three-dimensional vertical structures as will be shown later. Regarding the sectional values of the fluctuating lift coefficient, the distribution of this parameter along the cylinder length mirrors that of the fluctuating drag coefficient with the minimum values again occurring at the mid-plane except for the bare cylinder where that is where the maximum value occurs. The reduction in the centerline value relative to the bare cylinder is closer to 3.5 from 7.2 to 0.2. Taken together, the evidence from Figs. 10 and 11 suggest that the optimal value for H/L is in the range $0.5 < H/L < 0.66$.

The percentage reductions in the global mean and fluctuating force coefficients evaluated with respect to the bare cylinder values are presented in Fig. 12 where they are plotted for the range of H/L considered in this study. The consequences of adding the splitter plates are immediately obvious: the reduction in C_D sharply rises to 25% of the reference value for H/L in the range of 0–0.5, and there after the increase levels off suggesting limited further benefits at the expense of longer splitter plates. A similar trend is obtained in the reduction percentages of C'_D values which show an increase of 85% in the range of $0 < H/L \leq 0.33$, with no significant change beyond $H/L = 0.33$. Similarly, the percentage reduction in C'_l values rises to about 70% in the range $0 < H/L \leq 0.5$, again with little change for $H/L > 0.5$. Taken together, these results suggest an optimal plate height $H/L = 0.5$.

To better understand the processes leading to reduction of the global force coefficients with the addition of the splitter plates, and to quantify the extent to which three-dimensional effects are relevant in the configurations of interest, we examine the extent to which the vortex shedding from the entire length of the cylinder is correlated. Knowledge of the lengthwise correlation is also important in assessing the potential for

resonance which is increases with the extent to which shedding is closely correlated over a given cylinder length. To this end, the correlation coefficient (γ) appropriate to two fluctuating quantities occurring at different spanwise locations (X, Y) is evaluated from:

$$\gamma_{z_1 z_2} = \left(\overline{XY} - \overline{X}\overline{Y} \right) \Big/ \left(\sqrt{\overline{X^2}} \sqrt{\overline{Y^2}} \right)$$

The correlation coefficients were calculated at each time step and the results presented here are for when their values ceased to change with time. Since the fluctuating lift and drag are integrals of the fluctuating pressure, it was of interest to observe the lengthwise correlation of the fluctuating pressures at different angular locations (θ). To further condense the results, the average correlation coefficients were computed for one, two, three, four, five, six and seven monitoring spacing by taking the average values on the diagonals successively removed from the leading diagonal in the γ matrix. Fig. 13 shows the variation of spanwise correlation coefficient with length at three different locations around the circumference. It can be seen that γ of the bare cylinder is everywhere significantly higher than that of the cylinder with the optimal w/D and H/L proportions. A low value of γ at a given value of z/D indicates that the vortex shedding at that location is uncorrelated with that which occurs from the cylinder base. For the bare cylinder, and along the nominal stagnation line, γ drops to a value of 0.9 while the drop is much greater, to 0.42, along the base line. In contrast, for the cylinder with splitter plate, the correlation coefficient significantly decreases due to presence of the plate which effectively uncouples from each other the shedding processes that occur above and below it. Along the base line ($\theta = 180°$), the correlation coefficient is seen to become negative where, at the mid-plane ($z/D = 2.5$), it takes on the values of -0.2. Along the stagnation line, the minimum value of γ drops to 0.6 and then trends to become constant along the cylinder.

Contours of instantaneous vorticity, pressure and turbulence kinetic energy at three locations along the cylinder span are presented in Fig. 14. Results for both with and without splitter plates are presented, the former for the case of $w/D = 0.5$. The high degree of the spanwise correlation of
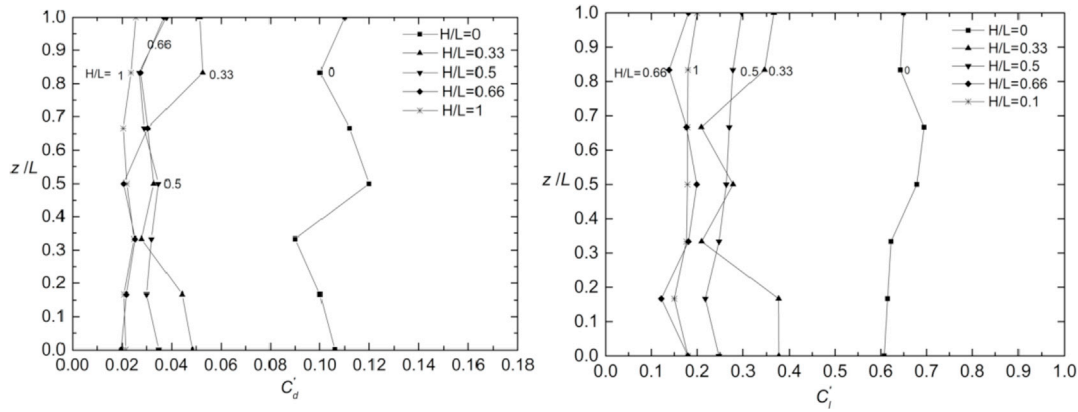
Fig. 11. Spanwise variation of sectional fluctuating drag (left) and lift (right) coefficients as a function of splitter plate length.
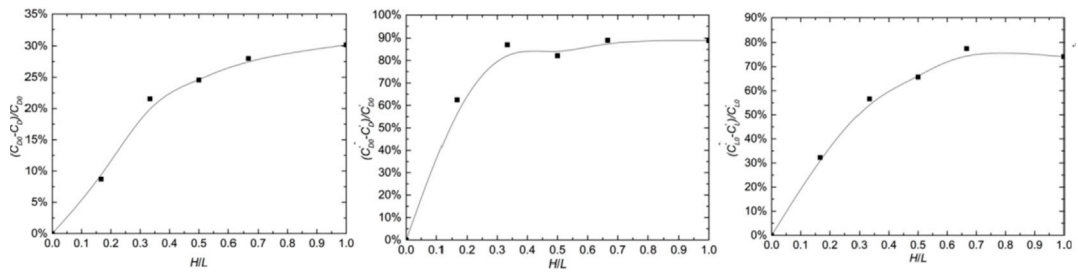

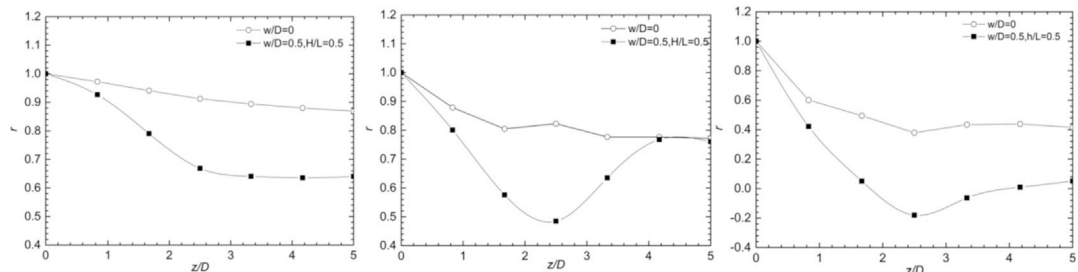**Fig. 12.** Percentage reductions of global mean and fluctuating force coefficients.

Fig. 13. Spanwise variation of fluctuating pressure correlation coefficients (respectively from the left for $\theta = 0°$, $\theta = 90°$ and $\theta = 180°$).

the vortex-shedding process for the case of the bare cylinder noted earlier is evident from all the contours presented in Fig. 14 where the contrast with the results for $w/D = 0.5$ are quite clear. Another consequence of the presence of the splitter plate is the reduction in the strength of the flapping mean-flow motion and hence in the rate of production of turbulence kinetic energy k. This manifests itself in the overall reduction in the levels of k, especially in the region immediately downstream of the cylinder. Further downstream, the levels of k actually increase due to the merger of the separated shear layers that develop on either side of the splitter plate.

The time history of the lift and drag coefficients are shown in Fig. 15. The effectiveness of the splitter plates in reducing the mean value of the drag coefficient and the fluctuations in both the lift and drag is clearly evident for all values of w/D in further confirmation that the global instability that manifests the vortex shedding is susceptible to small changes in the wake region that effectively uncouple the alternate formation of vortices from either side of the splitter plate. Fig. 15 also shows the extraordinarily large benefits that arise when a plate of optimal dimensions is employed.

Finally, by performing fast Fourier transforms on the time histories of the lift coefficient to obtain the power spectra, it was noted that well-defined peaks are obtained yielding the Strouhal numbers shown in

Fig. 16. The variation of this parameter with the width and length of the splitter plate is very small, its value remains close to that of a bare cylinder at similar Reynolds number.

4. Concluding remarks

While it is well established through experiments and computations that the attachment of a splitter plate to the base of a circular cylinder can reduce the strength of vortex shedding and hence the fluctuating forces on the cylinder, there is virtually no evidence of the effectiveness of this method at the high Reynolds numbers typically encountered in wind engineering, or reliable guidelines regarding the optimal ratios of splitter plate width to cylinder diameter and plate height to cylinder length. This study was accordingly performed to advance our understanding of the mechanisms for vortex suppression by splitter plates, and to quantify their dependence on the two geometric parameters that define the relation between the splitter plate and the cylinder namely the ratios of their respective dimensions in the direction of the flow, and in the direction along the cylinder axis normal to it. The computations were performed with an eddy viscosity model that has been adapted to account for the interactions between the periodic vortex shedding and the random turbulence. The need for this adaptation was demonstrated by comparisons
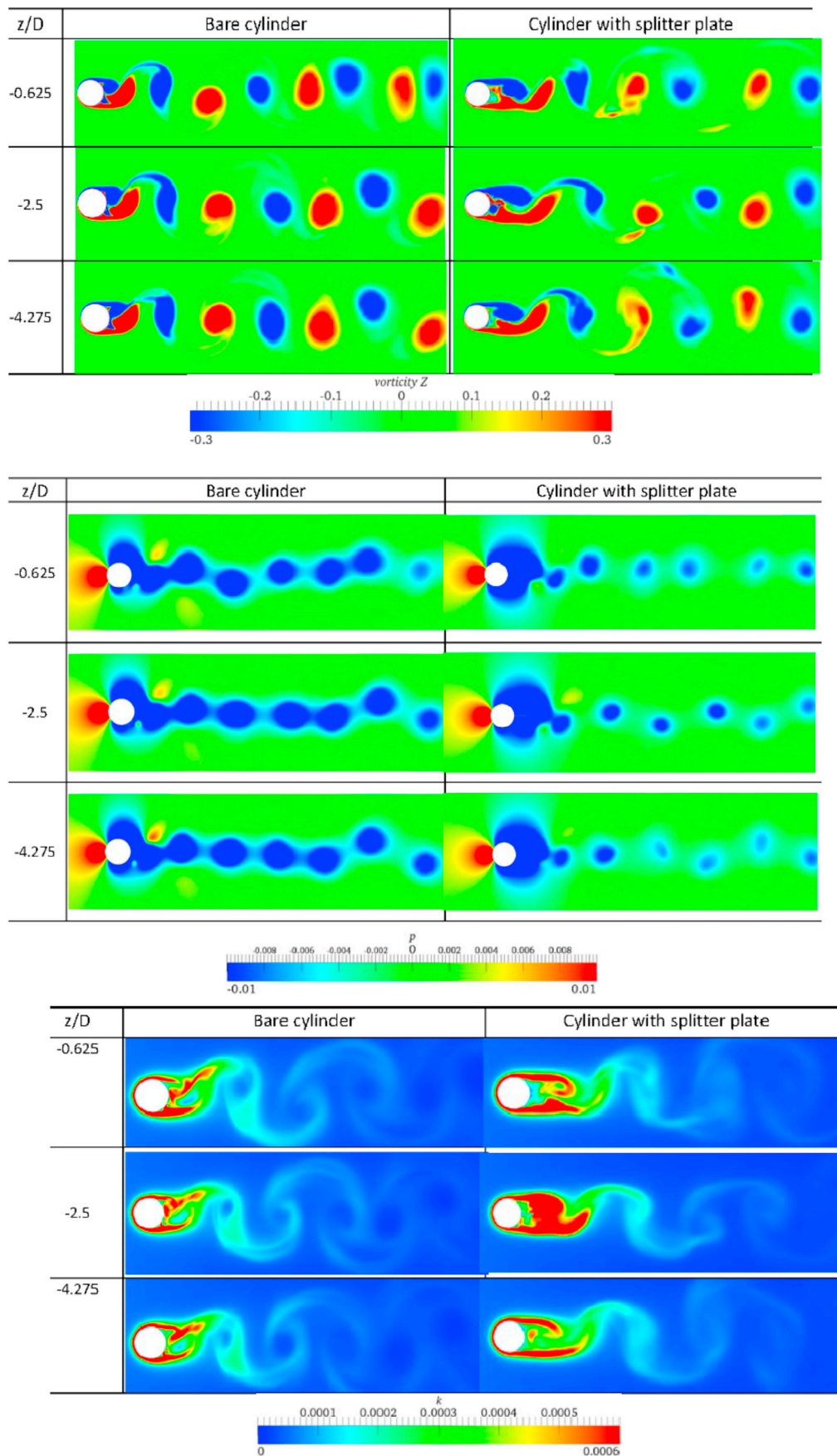
Fig. 14. Contours of mean vorticity (top), pressure (center), and turbulence kinetic energy (bottom) at various spanwise locations with and without splitter plate ($w/D = 0.5, H/L = 0.5, t^* = 68.9$).
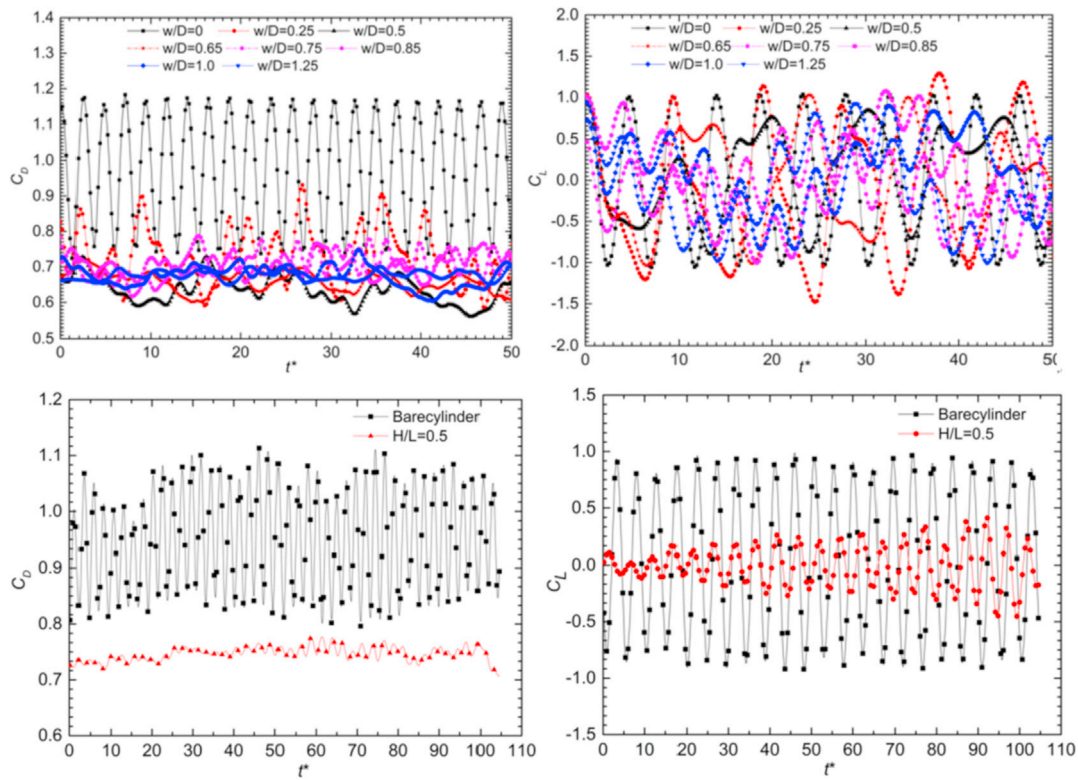
Fig. 15. Time history of the lift and drag coefficients showing dependence on w/D (top), and extent of reduction obtained with $H/L = 0.5$ (bottom).
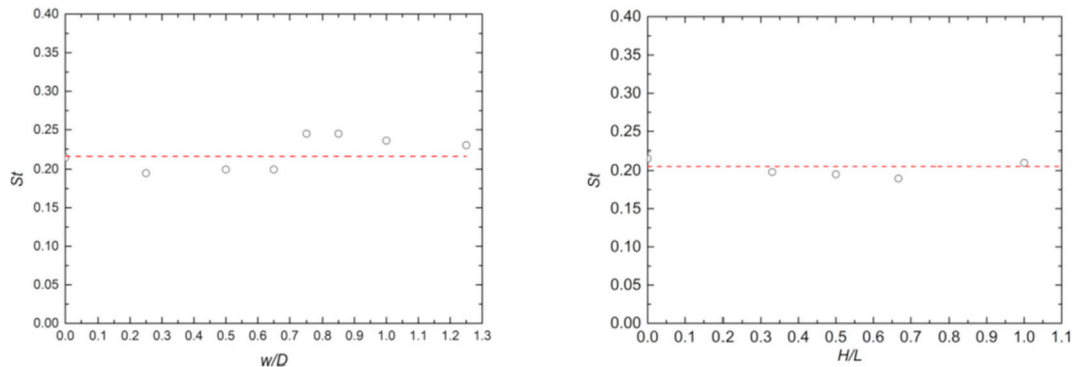

Fig. 16. Predicted variation of global St with w/D (left) and H/L (right).

with experimental data. The numerical accuracy was checked using the Grid Convergence Index method. In this regard, the present finding that a splitter plate having a width to cylinder diameter ratio of 0.66, and height to length ratio of 0.5 yields the greatest degree of suppression will serve in formulating practical guidelines for the deployment of splitter plates on structures in environments where the direction of the incident wind or current is constant and is known *a priori*.

Nomenclature

A	Projected area
B_f	Blockage ratio
D	Cylinder diameter
C_d, C_D	Time-averaged sectional and total drag coefficient
C_{drms}, C_{Drms}	Sectional and total fluctuating drag coefficient
C_{lrms}, C_{Lrms}	Sectional and total fluctuating lift coefficient
C_p, C_p'	Time-averaged and r.m.s. surface pressure coefficient

f_s	Frequency of vortex shedding
H	Plate height
k	Turbulence kinetic energy
L	Cylinder length
P_k	Production rate of turbulence kinetic energy
P_∞	Reference pressure (atmospheric)
Q	Mean-flow kinetic energy $= \left(\frac{1}{2}U_i U_i\right)$
Re	Reynolds number$\left(= \frac{UD}{\nu}\right)$
St	Strouhal number $\left(= \frac{f_s D}{U_0}\right)$
U_0	Velocity of incident flow
U_i	Mean velocity components
u_i	Fluctuating velocity components
u_τ	Friction velocity
$\overline{u_i u_j}$	Reynolds-stress tensor
w	Splitter plate width

Greek

δ_{ij}	Kronecker delta
Δt^*	Non-dimensional time-step $= \left(\frac{\Delta t\, U_o}{D}\right)$
Δn_c	Normal distance from the cell center to the wall
ε	Turbulence energy dissipation rate
κ	von Karman constant
μ	Dynamic viscosity
υ	Kinematic viscosity
υ_t	Eddy viscosity
ρ	Fluid density
γ	The correlation coefficient
θ	Circumferential angle

Subscripts

i,j	Cartesian tensor indices
o	Inlet value
∞	Reference value

References

Anderson, E.A., Szewczyk, A.A., 1997. Effects of splitter plate on the near wake of a circular cylinder in 2 and 3 dimensional flow configurations. Exp. Fluid 23 (2), 161–174.

Apelt, C.J., West, G.S., Szewczyk, A.A., 1973. The effects of wake splitter plates on the flow past a circular cylinder in the range $10^4 <$ Re$< 5 \times 10^4$. J. Fluid Mech. 61 (1), 187–198.

Batham, J.P., 1973. Pressure distributions on circular cylinders at critical Reynolds numbers. J. Fluid Mech. 57 (2), 209–228.

Blevins, R.D., 1990. Flow Induced Vibrations, second ed. Krieger Publishing Company, New York.

Bearman, P.W., Branković, M., 2004. Experimental studies of passive control of vortex-induced vibration. Eur. J. Mech. B Fluid 23 (1), 9–15.

Cantwell, B., Coles, D., 1983. An experimental study of entrainment and transport in the turbulent near wake of a circular cylinder. J. Fluid Mech. 136, 321–374.

Celik, I.B., Ghia, U., Roache, P.J., Freitas, C.J., Coleman, H., Read, P.E., 2008. Procedure for estimation and reporting of uncertainty due to discretization in CFD applications. J. Fluid Eng. 130 (7), 078001-1–078001-4.

Chen, W.L., Xin, D.B., Xu, F., Li, H., Ou, J.P., Hu, H., 2013. Suppression of vortex-induced vibration of a circular cylinder using suction-based flow control. J. Fluid Struct. 42, 25–39.

Choi, H., Jeon, W.P., Kim, J., 2008. Control of flow over a bluff body. Annu. Rev. Fluid Mech. 40, 113–139.

Dai, S., Younis, B.A., Sun, L., 2015. OpenFOAM predictions of hydrodynamic loads on full-scale TLP. Ocean Eng. 102 (1), 162–173.

Dai, S., Younis, B.A., Zhang, H.Y., 2017. Prediction of turbulent flow around a square cylinder with rounded corners. J. Offshore Mech. Arctic Eng. 139, 031804-1–031804-9.

Durao, D., Heitor, M., Pereira, J., 1988. Measurements of turbulent and periodic flows around a square-section cylinder. Exp. Fluid 6 (5), 298–304.

European Wind Energy Association Report, 2017. European Wind Energy Association Report, 2015. The European offshore wind industry – key trends and statistics. https://windeurope.org/wp-content/uploads/files/about-wind/statistics/WindEurope-Annual-Offshore-Statistics-2017.pdf. (Accessed 20 July 2018).

Feyzollahzadeh, M., Mahmoodi, M.J., Yadavar-Nikravesh, S.M., Jamali, J., 2016. Wind load response of offshore wind turbine towers with fixed monopile platform. J. Wind Eng. Ind. Aerod. 158, 122–138.

Franke, R., Rodi, W., 1993. Calculation of vortex shedding past a square cylinder with various turbulence models. Turbulent Shear Flows 8, 189–204.

Gu, F., Wang, J.S., Qiao, X.Q., Huang, Z., 2012. Fluctuating forces and vortex shedding behavior of circular cylinder with rotatable splitter plates. J. Fluid Struct. 28, 263–278.

Homescu, C., Navon, I.M., Li, Z., 2002. Suppression of vortex shedding for flow around a circular cylinder using optimal control. Int. J. Numer. Meth. Fluid. 38 (1), 43–69.

Kato, M., Launder, B.E., 1993. The modeling of turbulent flow around stationary and vibrating square cylinders. In: Proc. 9th Symp. Turbulent Shear Flows, Kyoto, 10.4.1–10.4.6.

Korkischko, I., Meneghini, J.R., 2012. Suppression of vortex-induced vibration using moving surface boundary-layer control. J. Fluid Struct. 34, 259–270.

Kwon, S.H., Cho, J.W., Park, J.S., Choi, H.S., 2002. The effects of drag reduction by ribbons attached to cylindrical pipes. Ocean Eng. 29 (15), 1945–1958.

Lecordier, J.C., Hanmma, L., Paranthoen, P., 1991. The control of vortex shedding behind heated cylinder at low Reynolds numbers. Exp. Fluid 10 (4), 224–229.

Murakami, S., 1993. Comparison of various turbulence models applied to a bluff body. J. Wind Eng. Ind. Aerod. 46–47, 21–36.

Norberg, C., 2003. Fluctuating lift on a circular cylinder: review and new measurements. J. Fluid Struct. 17 (1), 57–96.

Qiu, Y., Sun, Y., 2014. Effects of splitter plates and Reynolds number on the aerodynamic loads acting on a circular cylinder. J. Wind Eng. Ind. Aerod. 127, 40–50.

Rodríguez, I., Lehmkuhl, O., 2013. High performance computing of the flow past a circular cylinder at critical and supercritical Reynolds numbers. Procedia Engineering 61, 166–172.

Schumm, M., Berger, E., Monkewitz, P.A., 1994. Self-excited oscillations in the wake of two-dimensional bluff bodies and their control. J. Fluid Mech. 271, 7–53.

Tran, T.-T., Kim, D.-H., 2015. The platform pitching motion of floating offshore wind turbine: a preliminary unsteady aerodynamic analysis. J. Wind Eng. Ind. Aerod. 142, 65–81.

Tokumaru, D.T., Dimotakia, P.E., 1991. Rotary oscillating control of a cylinder wake. J. Fluid Mech. 224, 77–90.

Trim, A.D., Braaten, H., Lie, H., Tognarelli, M.A., 2005. Experimental investigation of vortex-induced vibration of long marine risers. J. Fluid Struct. 21 (3), 335–361.

Tsuchiya, M., Murakami, S., Mochida, A., Kondo, K., Ishida, Y., 1997. Development of a new k-ε model for flow and pressure fields around bluff body. J. Wind Eng. Ind. Aerod. 67–68, 169–182.

Unal, M.F., Rockwell, D., 1988. On vortex formation form a cylinder Part 1: the initial instability. J. Fluid Mech. 190, 491–512.

West, G.S., Apelt, C.G., 1993. Measurements of fluctuating pressures and forces on a circular cylinder in the Reynolds number range 10^4 to 2.5×10^5. J. Fluid Struct. 7 (3), 227–244.

Yeung, R.W., 2002. Fluid dynamics of finned bodies—from VIV to FPSO. In: Proc. 12th Int. Conf. Offshore and Polar Engineering, Kitakyushu, Japan, pp. 1–11.

Younis, B.A., Zhou, Y., 2006. Accounting for mean-flow periodicity in Turbulence closures. Phys. Fluids 18 (1), 018102.

Younis, B.A., Przulj, V.P., 2006. Computation of turbulent vortex shedding. Comput. Mech. 37 (5), 408–425.

Zdravkovich, M.M., 1981. Review and classification of various aerodynamic and hydrodynamic means for suppressing vortex shedding. J. Wind Eng. Ind. Aerod. 7, 145–189.